IOPscience iopscience.iop.org

Home Search Collections Journals About Contact us My IOPscience

Time-resolved radiation beam profiles in water obtained by ultrasonic tomography

This article has been downloaded from IOPscience. Please scroll down to see the full text article.

2010 Metrologia 47 208

(http://iopscience.iop.org/0026-1394/47/3/011)

View the table of contents for this issue, or go to the journal homepage for more

Download details:
IP Address: 129.6.99.122
The article was downloaded on 04/01/2011 at 15:41

Please note that terms and conditions apply.

IOP PUBLISHING METROLOGIA
Metrologia **47** (2010) 208–218 doi:10.1088/0026-1394/47/3/011

Time-resolved radiation beam profiles in water obtained by ultrasonic tomography

Eugene V Malyarenko[1,3], Joseph S Heyman[1,4], H Heather Chen-Mayer[2] and Ronald E Tosh[2]

[1] Luna Innovations Incorporated, 1 Riverside Circle, Suite 400, Roanoke, VA 24016, USA
[2] Ionizing Radiation Division, NIST, 100 Bureau Drive, Stop 8460, Gaithersburg, MD 20899, USA

E-mail: evmaly@yahoo.com

Received 10 December 2009, in final form 4 February 2010
Published 1 April 2010
Online at stacks.iop.org/Met/47/208

Abstract
This paper presents a practical ultrasonic system for near real-time imaging of spatial temperature distributions in water caused by absorption of radiation. Initial testing with radiation from a highly attenuated infrared lamp demonstrates that the system is able to map sub-millikelvin temperature changes, thus making it suitable for characterizing dose profiles of therapy-level ionizing radiation beams. The system uses a fan-beam tomographic reconstruction algorithm to invert time-of-flight data derived from ultrasonic pulses produced and detected by a circular array of transducers immersed in water. Temperature dependence of the speed of sound in water permits the conversion of these measured two-dimensional velocity distributions into temperature distributions that indicate the absorbed radiation dose. The laboratory prototype, based on a 128-element transducer array, is used to acquire temperature maps of a 230 mm × 230 mm area every 4 s with sub-millikelvin resolution in temperature and about 5 mm resolution in space. Earlier measurements with a single-channel version of this prototype suggest refinements in signal-conditioning electronics and signal-processing algorithms that would allow the present instrument to resolve temperature changes as low as a few microkelvin. Possible applications include real-time intensity profiling of radiation beams and three-dimensional characterization of the absorbed dose.

(Some figures in this article are in colour only in the electronic version)

1. Introduction

Intensity-modulated radiation therapy (IMRT) is the delivery of radiation to the patient via fields that have non-uniform radiation fluence [1], often used for the treatment of tumours in close proximity to normal organs or critical structures that are more sensitive to radiation. In addition to using multiple-shaped portals from which the radiation beams emanate, the intensity of the beams within each portal is spatially modulated using sophisticated software and hardware. This enables delivery of optimized dose distributions to the three-dimensional tumour volume while avoiding nearby or overlapping normal structures.

Measurement of the absorbed dose in tissue produced by such complex-shaped and dynamically changing beams is a challenging problem closely linked to the ability to assess and monitor spatial intensity profiles of the beam. The contrast between beam conditions employed in the treatment of patients via IMRT and those defining standard reference conditions is of growing concern within the dosimetry standards community and is directly related to the absence of primary reference standards that are suitable for assessing absorbed dose in IMRT-type beams. Among existing primary reference standards for assessing radiotherapeutic dose, calorimetric standards would appear to be the most suitable for obtaining time-resolved spatial distributions because they are constructed of a uniform, extended medium that could contain and faithfully register the spatial features of the beam over time.

Water calorimeters used in standard reference dosimetry [2] assess absorbed dose to water at a point in space using

[3] Current address: Tessonics Corp., 2019 Hazel St, Birmingham, MI 48009, USA.
[4] Current address: Applied Research Associates, New England Division, 130 Indian Springs Rd, Williamsburg, VA 23185, USA.

 © 2010 BIPM & IOP Publishing Ltd Printed in the UK & the USA

small, glass bead thermistors and are capable of registering sub-millikelvin temperature changes with a precision of about 0.1%. Such a design poses two major drawbacks: (1) thermistors and associated non-water materials perturb the temperature environment being measured and (2) the reference is only given at a point in space, and the method is not designed for profiling the spatial distribution of the absorbed dose. The first is a problem for temperature measurements in general and the second is for spatial dose mapping in particular.

In our previous work [3–5] we addressed problem (1), above, by developing a single-channel ultrasonic thermometer [6] that registers minute, radiation-induced temperature changes inside a water phantom without introducing foreign materials into the water. With a 3.2 μK root-mean-square (RMS) sensitivity, it can compete with the existing thermistor-based technology. The system was used to obtain accurate estimates of absorbed dose to water averaged over the flight path of the ultrasonic tone burst that traverses the entire length of the phantom.

In this paper we address problem (2) with the design and implementation of a two-dimensional ultrasonic thermal imaging system that employs this high-precision ultrasonic technology within a tomographic data acquisition scheme. This approach is made feasible by the small thermal diffusivity of water ($\kappa = 1.4 \times 10^{-7}\,\mathrm{m^2\,s^{-1}}$ at room temperature), which enables spatial temperature profiles induced by absorbed radiation to remain effectively undistorted by heat conduction for several seconds. The expansion in the number of channels required by the tomographic scheme necessarily increases the overall acquisition time above that required by the single-channel system, raising the possibility that heat transport would significantly degrade the measurements. Nevertheless, as we shall describe below, it was possible to avoid this problem with a modest sacrifice in temperature resolution.

There has been much work on non-dosimetry applications combining precision ultrasonic thermometry with computed tomography [7, 8]. While sub-millikelvin sensitivity has not been previously reported, the earlier work nevertheless suggests that high temperature resolution is possible in a wide variety of thermal environments. For example, by measuring travel-time variations of acoustic signals, tomography has been used to reconstruct large-scale temperature structure within the ocean [9, 10], where, despite the widespread occurrence of perturbations (due to variations in salinity, the presence of gas bubbles, multiple reflections from top and bottom surfaces and other factors that deflect acoustic rays from straight-line paths), a temperature resolution of 3.8 mK has been reported [10]. Such precision is achievable mainly due to long propagation distances in the ocean that amplify the effect of water temperature changes on the acoustic arrival time. A tomographic approach was also used to visualize temperature profiles due to Rayleigh–Benard convection in glycerol [11]. The reported temperature resolution (standard deviation) was 0.16 K.

Ultrasonic techniques have been previously used for measuring absorbed radiation dose in gels [12–14] and acrylic plate (polymethyl methacrylate or PMMA) [15] in which ionizing radiation causes chemical and physical changes that are detectable by transmission ultrasound computed tomography for obtaining two-dimensional dose distributions. These systems use the same detection principle that is employed in the well-developed area of ultrasound diagnostic imaging where tissue parameters are discerned [16]. Often both the amplitude and phase are utilized, especially when structural changes are involved. It is worth pointing out that the observed effects in these systems are associated with irreversible changes in material properties due to the ionizing radiation. Our system detects the change in the speed of sound directly caused by radiation-induced temperature changes in water, rather than permanent structural changes probed by the other techniques. Both types of technique detect changes in the speed of sound, V, due to deposition of radiant energy into the medium, and therefore both can assess the radiation dose, but, whereas the structural changes are material dependent and must be calibrated, the temperature change in water is a direct realization of the absorbed dose.

As might be expected, the instrumental sensitivity required to assess dose by means of these various mechanisms and materials varies considerably. The effective sensitivity, measured as the fractional change in speed of sound, $\Delta V/V$, per gray ($1\,\mathrm{Gy} = 1\,\mathrm{J\,kg^{-1}}$), was reported to be $2.7 \times 10^{-4}\,\mathrm{Gy^{-1}}$ in gel [13], sufficient for their instrument to measure therapy levels of a few gray. For the PMMA work [15], an effective sensitivity of about $2.7 \times 10^{-8}\,\mathrm{Gy^{-1}}$ puts the measurable radiation doses for their instrument in the kilogray region, appropriate for industrial irradiation applications but not for medical radiotherapy. The change due to temperature rise in water by the same type of radiation is about $5 \times 10^{-7}\,\mathrm{Gy^{-1}}$, three orders of magnitude lower than gel, therefore requiring a much more sensitive instrument.

The instrument we developed in our previous mono-channel work [3, 5] can discern $\Delta V/V$ as small as 7×10^{-9}, corresponding to 3.2 μK, and thus it is sufficiently sensitive for dosimetry of therapy-level radiation. This work, based upon a two-dimensional implementation of our earlier high-sensitivity single-channel ultrasonic thermometer, achieves sub-millikelvin resolution for tomographic reconstructions of temperature distributions induced by radiation in a uniform medium of water. The tomographic reconstruction provides a snapshot of the temperature distribution in the irradiated medium, offering a direct dose map even for complicated beam geometries. The temperature resolution of our experimental results exceeds that found in the literature and indicates that the technique has considerable promise for evaluating real-time 3D dose profiles in a clinical setting.

2. Materials and methods

2.1. Acoustic tomography in water

Single-channel, pulsed ultrasonic thermometers [5, 8] typically are designed to measure temperature changes indirectly by their influence upon the attenuation or propagation speed of an ultrasonic probe pulse. If local temperature variations $\Delta T(\vec{r})$ are sufficiently small that the relationship between temperature and measured quantity is effectively linear, a

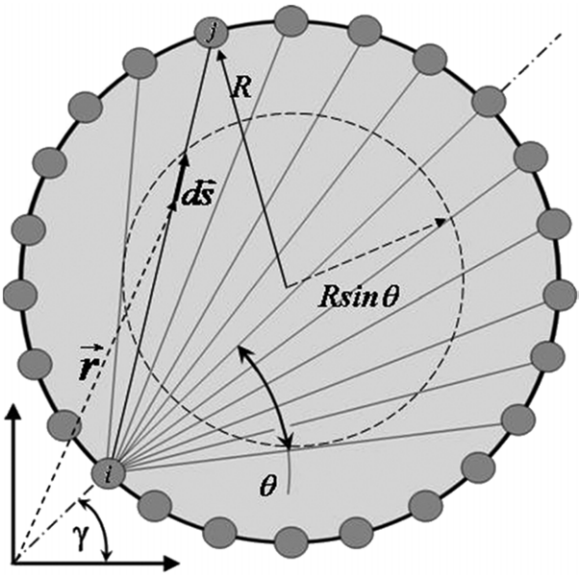

Figure 1. Fan-beam data acquisition with circular transducer array.

single measurement of the pulse after passage through the medium yields an average temperature change along the acoustic path L_{ij} connecting the transmitting (i) and receiving (j) transducers:

$$\overline{\Delta T}_{ij} = \frac{1}{L_{ij}} \int_i^j \Delta T(\vec{r})\, \mathrm{d}\vec{s}. \tag{1}$$

By utilizing a suitable array of transmitters and receivers, such measurements can be carried out in a way that permits the inversion of equation (1) to obtain spatially resolved temperature distributions throughout the probed volume. Efficient reconstruction procedures have already been developed in medical x-ray and ultrasound tomography for certain data acquisition geometries. In this work we adopted a circular, fan-beam data acquisition geometry where the reconstructed area is a circle defined by radius R, and ultrasonic transducers capable of both detecting and transmitting ultrasound are placed at equal intervals along the circumference. One tomographic projection contains the acoustic phase-change data extracted from signals propagating between a given transmitter and a corresponding fan-like bank of receivers (figure 1). The mathematical description of reconstruction algorithms for the fan-beam data acquisition scheme can be found in [17]. For the sub-millikelvin temperature changes in water that are being considered here, straight-line trajectories between transmitters and receivers may be safely assumed.

As shown in figure 1, the ultrasonic wave field (tone burst) spreading from the given transmitter $\boldsymbol{i}$ into the effective opening angle 2θ is collected by an equiangular array (fan) of receivers on the opposite side of the circular array. The ultrasonic signal detected by each receiver $\boldsymbol{j}$ within the fan is processed in order to extract the average temperature change $\overline{\Delta T}_{ij}$ (equation (1)) along the acoustic path specific to the particular transmitter–receiver pair $\boldsymbol{ij}$. The collection of values $\overline{\Delta T}_{ij}$ for all receivers $\boldsymbol{j}$ within the fan corresponding to the transmitter $\boldsymbol{i}$ defines a single tomographic projection; multiple projections are obtained by incrementing the transmitter number and shifting the fan accordingly.

While such a system is capable of evaluating the temperature distribution within the volume enclosed by the transducer array, the best reconstruction quality is obtained within the subvolume that is probed by all of the projections. This subvolume is defined by a region whose periphery is traced out by the two outermost rays as the fan formed by a single transmitting transducer and the bank of receiving transducers is scanned around the transducer ring. Only the functionality (transmitting/receiving) of the transducers is scanned; the transducer ring remains stationary. In the present case, the subvolume would lie within a circle that is concentric with the circle of radius R containing the transducers but having a reduced radius of $R \sin\theta$ (see figure 1). Spatial resolution of the reconstructed distribution is limited by the number of transducer elements, which was determined by computational modelling as described in the following section.

2.2. Reconstruction of simulated two-dimensional temperature profiles

To estimate the number of transducers in the circular array required for the desired spatial resolution, we applied the fan-beam reconstruction algorithm to a simulated thermal distribution. The temperature profile within the radiation beam was modelled as three concentric elliptical regions uniformly heated to different temperatures. For each transmitter–receiver pair the simulated effect was made to be proportional to the phase change of the acoustic pulse due to heating and calculated as described below.

In water, the speed of sound under constant atmospheric pressure and concentration of impurities depends only on the temperature and can be approximated by the empirical formula [18]:

$$V(T) = c + bT + aT^2, \tag{2}$$

where $V(T)$ is the speed of sound ($\mathrm{m\,s^{-1}}$) at temperature T (°C), $c = 1405.03\,\mathrm{m\,s^{-1}}$ is the speed of sound at 0 °C, $b = 4.624\,\mathrm{m\,(s\,^\circ C)^{-1}}$ and $a = -0.038\,\mathrm{m\,(s\,^\circ C^2)^{-1}}$.

Our model assumed a uniform equilibrium temperature of T_0 everywhere in the water tank before heating and a temperature increase inside the ith ellipse of ΔT_i after heating (figure 2). For sufficiently weak temperature disturbances $\Delta T_i \ll T_0$ we can estimate the contribution of each elliptical region to the total phase change incurred by the acoustic signal:

$$\Delta\varphi_i = \Delta\left(\omega\frac{S_i}{V}\right) = -\omega\cdot S_i\frac{\Delta V_i}{V_0^2} = -\omega\cdot S_i\cdot(b+2aT_0)\,\frac{\Delta T_i}{V_0^2}, \tag{3}$$

where ω is the centroid (angular) frequency of the ultrasonic probe pulse, V_0 is the sound speed at $T = T_0$ and S_i is the length of the acoustic path segment within the ith ellipse. By defining a contrast coefficient $\alpha = -\omega\cdot(b+2aT_0)/V_0^2$, we obtain $\Delta\varphi_i = \alpha\cdot S_i\cdot\Delta T_i$.

The total phase change accumulated by the wave after propagating through the heated area is obtained by adding the

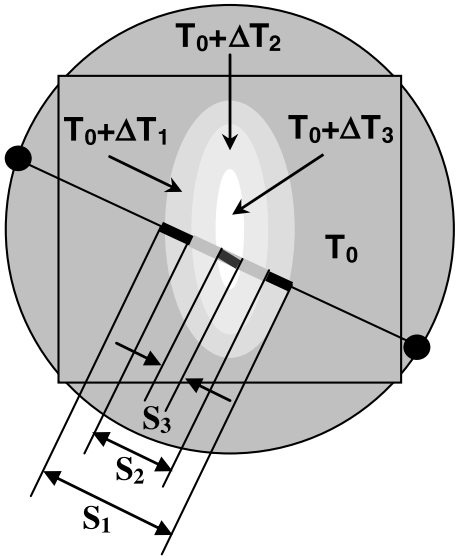

Figure 2. Modelling radiation-induced thermal profile in water as a combination of elliptical regions heated to different temperatures.

effects of all embedded elliptical regions:

$$\Delta\varphi = \alpha \cdot \sum_{i=1}^{3} S_i(\Delta T_i - \Delta T_{i-1}), \tag{4}$$

where $\Delta T_0 = 0$, and segment lengths S_i for given acoustic path are computed analytically for all ellipses.

Spatial parameters for the simulations were chosen to approximate corresponding conditions in the actual experiment. The image size was chosen to be 300 × 300 pixels. For the transducer array of radius R, the vertical and horizontal semi axes of the largest ellipse were $a = 0.36R$ and $b = 0.16R$. Two smaller ellipses were embedded in the largest one with size decrements $\Delta a = a/4$ and $\Delta b = b/4$. Phase shifts were calculated using (4) with $\alpha = 1$ and $\Delta T_i = 1, 2, 3$. The fan-beam opening angle was set to 90° as the maximum practical value expected in our experimental setup. This defined the number of receivers in the fan as $N/2$, where N is the total number of transducers in the circular array. Thus, by varying N and holding all other parameters in the system fixed, we effectively varied the spatial resolution.

Figure 3 demonstrates the reconstruction of three embedded ellipses with $N = 32, 64, 128$ and 256. By visually comparing these four images we concluded that a 128-element array provides a reasonable balance between quality of the reconstruction and the size (cost) of the array.

The spatial resolution of a particular tomographic inversion method can be defined as the size of the smallest object reconstructed with acceptable accuracy. The resolution depends on many factors including the number of projections and rays per projection, the ultrasonic wavelength, etc. Physical properties of the object, such as shape, homogeneity and acoustic impedance, should also be taken into account when designing the imaging system. It is a common practical rule of thumb to use at least as many pixels in the reconstructed image as there are receivers in the fan. Accordingly, a simple estimate of the spatial resolution is obtained from the ratio of image size to the number of active receivers in each projection, both of which are determined by the opening angle and the radius of the circular transducer array. The 128 transducers spaced around the circle of radius R give a linear spacing of $2\pi R/128$. For $R = 177.8$ mm, this spacing is 8.7 mm. For a given fan, the arc length at the circumference is about twice that at the centre, and therefore the resolution at the centre may be taken as about 1/2 of the transducer spacing along the circumference, or 4.4 mm. We should also note that although increasing the number of pixels by using interpolation does not increase the effective resolution, it does give the images a smoother appearance. All our subsequent results are represented as 300 pixel × 300 pixel images.

The foregoing estimates neglect the spatial blurring of temperature distributions caused by heat conduction; accordingly, the effective spatial resolution of the measurement degrades with acquisition time. Solution of the heat equation [19] indicates that a point temperature disturbance in water spreads to radius r with a characteristic time constant of $r^2/4\kappa$, where κ is the thermal diffusivity of water ($\kappa = 1.4 \times 10^{-7}$ m^2 s^{-1} at room temperature). Thus, to prevent blurring in excess of 2.5 mm (or 50% of our estimated ideal spatial resolution) acquisition of all projections would have to occur within about 10 s. This constraint guided the design of the data acquisition system, which, along with other hardware comprising our prototype, is described below.

2.3. Experimental setup

The functional setup of the ultrasonic transducer array-based system for radiation beam cross-section imaging is shown in figure 4. A 128-element, 355.6 mm diameter circular transducer array is placed into a 457.2 mm diameter, 64.35 L cylindrical water tank surrounded by a foam insulation jacket. A 12-cycle 1 MHz harmonic tone burst signal from the Agilent 33220A function generator is amplified with a custom Luna RF Power Amplifier and sent to the array via a National Instruments SCXI-1130 256-channel multiplexer (MUX) configured with 2 × 128 switching topology. The received ultrasonic echoes after the MUX and a 45 (dB) Panametrics™ ultrasonic pre-amplifier are digitized with a 100 MHz, 14-bit Signatec PDA14-100 analogue-to-digital converter (ADC) and saved for post-processing.

Accurate phase measurements are affected by trigger jitter due to improper synchronization of different modules. To minimize jitter in our system we employed a custom clock divider that converted the 100 MHz clock output from the ADC to a 10 MHz external clock signal for the function generator. Custom LabVIEW software was used to extract phase information from the digitized ultrasonic waveforms and feed it into the tomographic reconstruction routine.

The temperature changes in the water tank are produced with a heat lamp controlled by an R165 relay board (National Control Devices). In the laboratory implementation presented in this work we used a 375 W Sylvania light bulb with an infrared reflector. The lamp was mounted in a sliding fixture over the water tank. The IR light beam was collimated with a cylindrical tin screen around the lamp to block side radiation

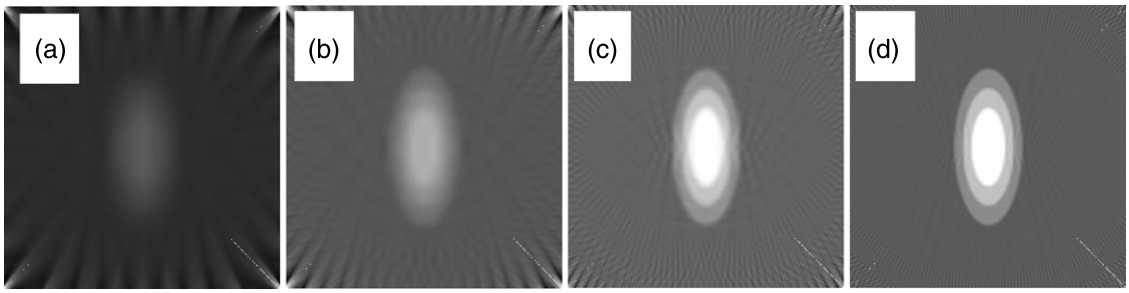

Figure 3. Reconstruction of simulated thermal distribution represented by three embedded ellipses, each at a slightly different temperature, using different numbers (N) of fan beams in the circular array. Each fan beam is sampled by half of the total number of virtual transducers in the array. (a) $N = 32$; (b) $N = 64$; (c) $N = 128$; (d) $N = 256$.

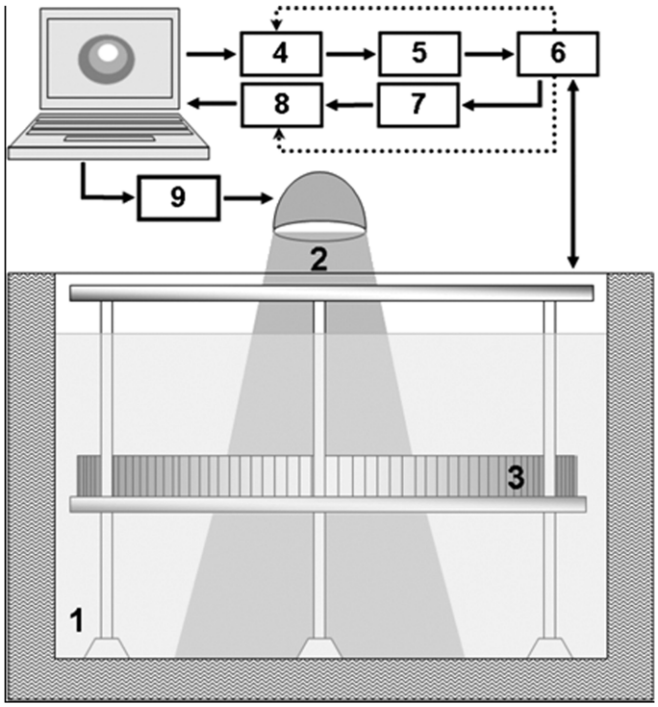

Figure 4. Functional setup of the ultrasonic transducer array-based system for radiation beam cross-section imaging. (1) Water tank in foam insulation; (2) relay-controlled light radiation source; (3) circular transducer array; (4) Agilent 33220A function generator; (5) Luna RF Power Amplifier; (6) NI SCXI-1130 2 × 128 multiplexer; (7) 45 dB Panametrics™ UT pre-amplifier; (8) Signatec 100 MHz, 14-bit ADC; (9) R165 Relay control board. Dashed lines designate trigger and timing. Custom LabVIEW software extracts phase information from digitized ultrasonic waveforms and feeds it into the tomographic reconstruction module.

and direct it into a 75 mm diameter aperture at the bottom of the tank. Assuming a luminous efficiency of about 5% and transmission efficiency through the collimation system of about 10%, the incident radiant power at the top surface of the water would be about 2 W. With the measured volume located between 8 cm and 10 cm depth in the phantom, Lambert–Beer attenuation by the water would lead to an estimate [20][5] of the rate of energy deposition into the detection layer of about 1 mW cm^{-3}, corresponding to an average expected rate

[5] Here we have made the simplifying assumption that the light from the lamp has a wavelength of about 1 µm, and have applied a Lambert absorption coefficient of 0.36 cm^{-1} in accordance with [20].

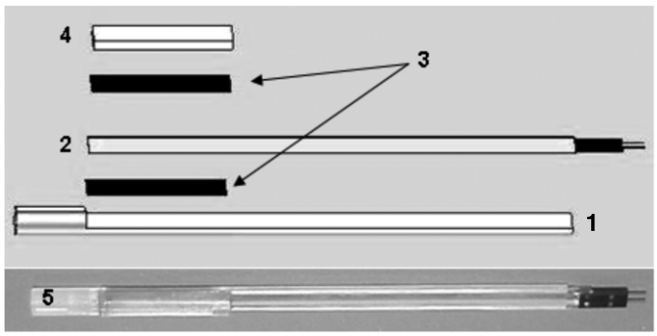

Figure 5. Ultrasonic transducer design. (1) Rexolite™ acoustic lens; (2) PVDF film with connector; (3) adhesive layers; (4) transducer backing; (5) photograph of an assembled array element.

of temperature increase of about 240 µK s^{-1} in the irradiated region, equivalent to the effect of 1 Gy s^{-1} of absorbed gamma radiation in water.

Previous studies with our single-channel ultrasonic thermometer indicated that such temperature signals would be easily detectable, because instrumental noise of ∼(4–5) µK RMS was quite low by comparison and because heat input by the ultrasonic transducer, estimated to be 7.2 µW within a detection volume of about 30 cm^3 of water, would contribute a negligible trend of ∼0.06 µK s^{-1} to the temperature waveform (the latter estimate was obtained by scaling measurements of electrical power dissipation in the transducer by the pulse duty cycle and transmission coefficient through the acrylic wall of the phantom). The present system, which uses a different transducer type and excitation circuitry, dissipates 5 mW acoustic power in a cylindrical volume of 710 cm^3 leading to the estimated heating rate of 1.69 × 10^{-6} K s^{-1}, which is only 0.7% of the estimated heating rate of the heat lamp. In either case, the observed thermal drift in the laboratory can be comparable to or exceed these small values. As long as the drift is quasi-linear within the radiation exposure period (tens of seconds), it can be approximated as a linear background in time and easily subtracted to obtain accurate temperature rise values.

The ultrasonic array was custom built from 128 laminated dual 110 µm polyvinylidene fluoride (PVDF) elements equipped with two-pin connectors (figure 5). The height of the active area of each PVDF element was 29.5 mm. Each element was bonded to a cylindrical acoustic lens machined out of a 5/16″ (7.9 mm) Rexolite™ rod and to a Mylar backing layer

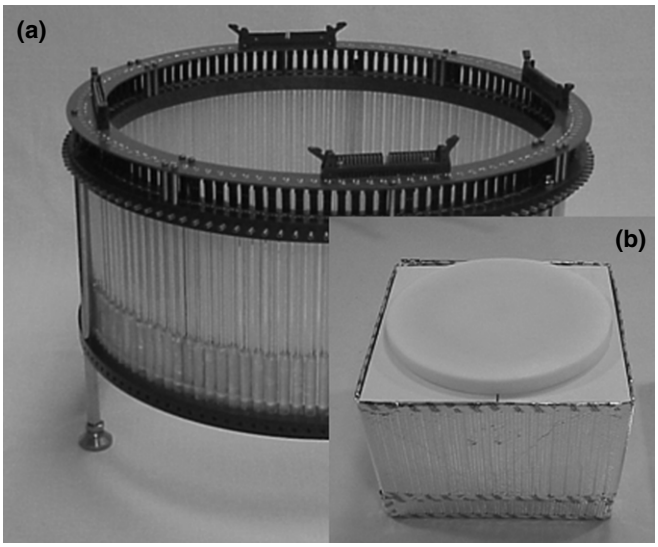

Figure 6. Components of the laboratory thermal imaging system: (*a*) 355.6 mm diameter, 128-element submersible ultrasonic array; (*b*) cylindrical water tank in foam insulation jacket with the cover on.

to damp unwanted reverberations. The elements were sealed with liquid silicone spray. This design allows for transducer immersion for up to 100 mm depth while keeping the connector above the water surface. The design of the acoustic lens allows transmitting ultrasonic waves between two transducers at up to 45° away from the normal on both sides. This allows for a 90° fan-beam opening angle. However, since this design does not maintain the same signal-to-noise ratio (SNR) for all rays in the fan, we are currently using only a 63.3° opening angle with 45 instead of 64 rays in the fan.

Figure 6 shows practical implementation of the transducer array. All 128 elements are harnessed together with two polyvinyl chloride (PVC) hoops. The bottom hoop has three threaded legs for height adjustment. The whole assembly rests on the bottom of the tank. The contacts of all transducer elements are inserted into mating connectors evenly distributed on a routing polychlorinated biphenyl (PCB) ring. The ring has four 50-pin ribbon-cable connectors on the top that group the contacts together to facilitate handling and addressing. The four ribbon cables connect the array to the SCXI-1130 MUX. At testing time, the array is usually partially submerged in the water leaving the top hoop, printed circuit board and all connectors dry. Its internal diameter of 355.6 mm can accommodate a standard ^{60}Co radiation beam of up to 200 mm × 200 mm cross section.

2.4. Data acquisition and signal conditioning

Our 64-projection, 45 rays-per-projection setup involves a total of 2880 individual waveform acquisitions. With each transmitted probe pulse having a duration of about 15 µs, acquisition of such a 64-projection scan would consume about 50 ms if done in serial (a necessity imposed by the present hardware, which did not permit ready separation of waveforms from different transducers that overlap in the time domain). To this we must add the aggregate propagation time of the ultrasonic pulses and time limits posed by scanning hardware. The transit time for a single pulse at the diameter is about 240 µs; thus, propagation delays would add no more than 0.7 s. The slowest hardware component was the mechanical switch module, which is limited to 900 Hz; thus, delays in the data acquisition system allowed images to be collected at a minimum period of 4 s.

Data throughput for imaging applications is often sufficiently high that special considerations should be given to possible bottlenecks in the data pipeline. In order to simplify the triggering scheme for data acquisition, each waveform was collected for the same duration (∼164 µs) and occupied (at the 100 MHz sampling rate) 16 384 16-bit words (32 kB) in computer memory. Because of the 900 Hz switching speed, the net data rate from the ADC to computer memory did not exceed 30 MB s^{-1}, which is well below the maximum transfer rate of the computer bus (128 MB s^{-1}). As noted above, all filtering and analysis of the data were done offline, in order to minimize interference with data transfer between the computer and the instruments.

Thus, whereas the data throughput required to process single probe pulses per transmitter/receiver pair appeared to be feasible with one computer alone, the latter was not believed to be sufficient for handling the additional throughput required for significant signal averaging (of multiple pulses per transmitter/receiver pair). In the single-channel instrument, noise was reduced from ∼400 µK (peak-to-peak) to less than 30 µK (peak-to-peak) (5 µK RMS) by averaging hundreds of pulses per measurement; thus, noise levels in the acquired waveforms from the present multichannel instrument were expected to approach 400 µK (peak-to-peak). However, an altogether unexpected noise was found on these waveforms that far exceeded the magnitude of the signal pulses. Closer inspection of the spectrum (figure 7(*b*)) of an example waveform, shown in figure 7(*a*), reveals that the spectral density of noise was concentrated in narrow bands around the 390 kHz frequency and some of its harmonics, most likely due to electrical pickup from a clock or switch. By contrast, the spectrum of the useful signal was localized around 1 MHz. Various efforts to suppress the noise via shielding of conductors and elimination of possible ground loops were unsuccessful; however, with the somewhat fortuitous separation of signal and noise found in the frequency domain, we were able to use digital band-pass filtering to extract the desired phase information with a much higher precision than might have been anticipated from casual inspection of the time-domain waveforms alone. In particular, using a LabVIEW zero-phase filter with a passband of 100 kHz around 1 MHz (shown in figure 7(*b*)), the waveform of figure 7(*c*) was obtained from the noisy waveform shown in figure 7(*a*). The zero-phase filter was selected in order to minimize phase distortion of the output, which introduces error into experimental estimates of time-of-flight and, hence, temperature.

2.5. Phase extraction and tomographic reconstruction

Filtered waveforms for each fan beam were analysed for temperature-induced changes of time-of-flight using the dual-reference heterodyning technique we originally developed

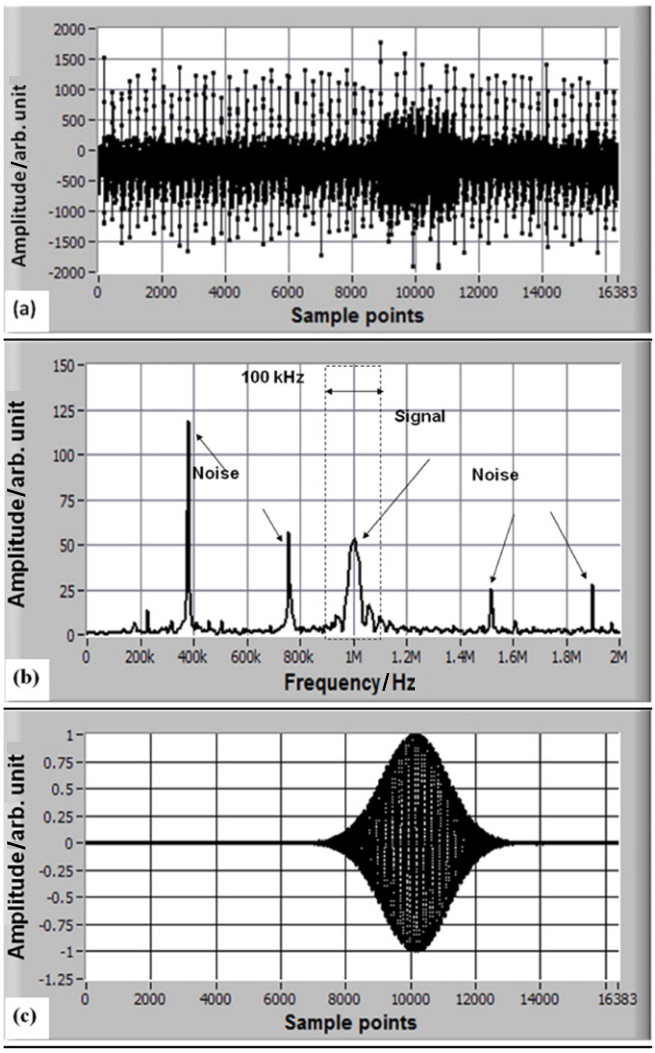

Figure 7. (*a*) Raw digitized 1 MHz acoustic signal between two elements on the opposite sides of the ring array (central ray of the fan beam). The SNR in the fan-beam signals gradually decreases away from the central ray; (*b*) spectrum of the raw signal (0 MHz to 2 MHz interval shown); (*c*) 1 MHz acoustic waveform after digital filtering with a 0.93 MHz to 1.03 MHz LabVIEW zero-phase band-pass filter.

for the digital phase-monitor (DPM) instrument previously described [5]. This approach registers very small (10 ps) changes in time-of-flight by their effect on the phase of the received waveform with respect to the phases of two reference waveforms. The flow charts in figure 8 indicate how this procedure compares with two other widely used techniques, Hilbert transformation and single-reference interference. While these other two techniques offer certain advantages with regard to computational simplicity and speed, the dual-heterodyning approach of figure 8(*c*) was found to be the most stable algorithm against perturbations due to noise and variations of signal shape observed with our transducer arrangement.

Phase data from each transmitter/receiver pair taken with and without incident radiation were then subtracted, smoothed and removed of outliers that could seriously affect reconstruction quality. The resulting phase projection data

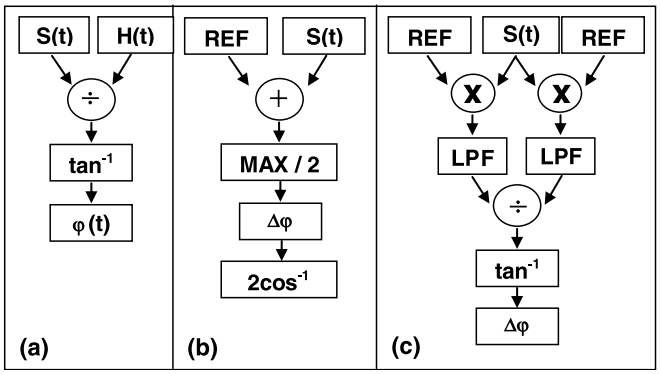

Figure 8. Three phase extraction algorithms used in this work. (*a*) Hilbert transform based algorithm; (*b*) algorithm that uses addition of a reference signal; (*c*) algorithm that uses heterodyne mixing with two phase-shifted reference signals. 'LPF' stands for the low-pass filter.

were then inverted using a filtered backprojection (FBP) algorithm [17].

3. Results and discussion

This section presents experimental results obtained from the ultrasonic array described above. Several tests were conducted with the light beam directed along the axis of the phantom with the objective of quantifying temperature increase in the water and observing evidence of heat transport, as conduction and convection processes would act in response to thermal gradients.

Figures 9(*a*) and (*b*) show tomographic surface plots of temperature profiles in the water tank obtained before and after 30 s exposure to the light beam. The *Z*-axis of these plots represents temperature change (kelvin) compared with a reference measurement taken shortly before the exposure. The total span of all the images shown in the *XY* plane is 230 mm × 230 mm (300 pixels × 300 pixels). Non-uniform intensity within the fan beam caused a significant decrease in the SNR from the centre to the periphery of the fan beam, which resulted in reconstruction artefacts—the elevated annulus evident in both surfaces—near the periphery. The decrease in the SNR towards the periphery is caused by decreasing intensity of the acoustic field away from the fan-beam centreline since the field radiated by the curved PVDF transducers is not perfectly cylindrical. This decreased the useful area of the tomographic reconstruction window to a 120 mm diameter circle, which constitutes a relatively artefact-free zone that can be used for quantitative measurements of sub-millikelvin temperature changes with the nominal spatial resolution.

Figure 10 compares two sets of measurements, each of which consists of linear temperature profiles across the diameter of the tank before (beam off) and after heating (beam on), retrieved from the data shown in figure 9. The first set was obtained with the light beam directed along the central axis of the phantom. The flat 120 mm long segment in the centre of the black curve (before heating) represents the low-noise area that provides meaningful temperature measurement results. Outside that region, reconstruction artefacts overwhelm the

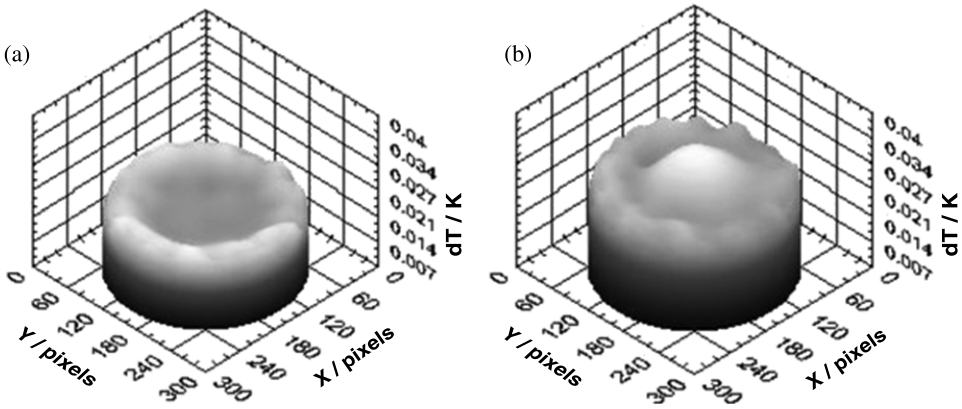

Figure 9. Temperature profile reconstructions in a water tank from a fan-beam tomographic acoustic experiment with 64 projections, 45 rays per projection. (*a*) The radiation source (heat lamp) off; (*b*) radiation source on for 30 s. Area dimensions: 300 pixels × 300 pixels (230 mm × 230 mm); the relative height of the temperature dome is approximately 9 mK.

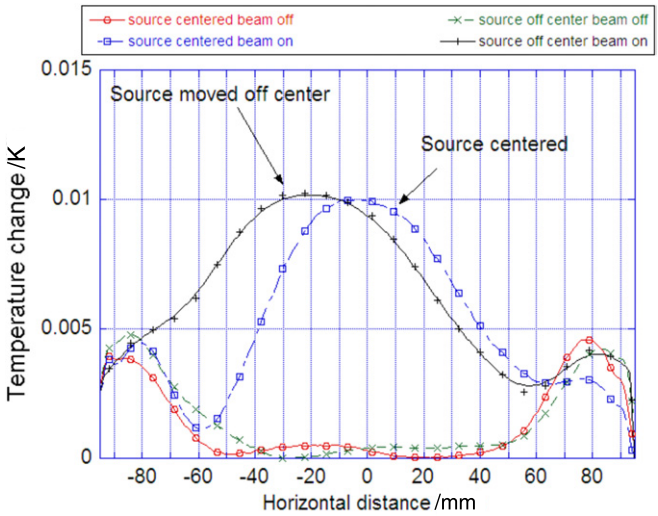

Figure 10. Linear temperature profiles in the water tank retrieved from the 2D tomographic reconstructions of the same area prior to heating (the bottom two curves) and after 30 s exposure to incandescent light (the top two curves). As indicated, the temperature response tracks the light source when it is moved off centre. The peripheral features beyond ±80 mm from the centre are reconstruction artefacts.

temperature distributions (however, at ±80 mm from the centre it is cut off by a flat-top, tapered cosine window designed to improve readability of the reconstructed images). The fact that the side lobes are indeed caused by the low SNR on the periphery of the beam is readily confirmed by examining the baseline datasets (the bottom two curves in figure 10) acquired before the heat source was turned on. The side lobes are present in those curves and grow in amplitude towards the periphery of the image. However, starting at ±80 mm from the centre this growth is suppressed by the aforementioned apodization window. The difference in height at the centre between the two profiles in figure 10 is approximately 9 mK, consistent with the estimated rate of temperature increase, given above, for a 30 s exposure. The post-processed noise, which gives an indication of the temperature sensitivity within the 120 mm diameter central area, is in the sub-millikelvin range.

The second set of curves was obtained with the heat lamp translated 25 mm to 30 mm away from the central axis of the tank. As expected, the maximum of the temperature distribution shifted accordingly. Otherwise, the heat buildup in the system is similar to the previous set. This test demonstrates how the measurement noise on the periphery of the fan beam (e.g. on the left hand side of the off-centre curve, figure 10) can be offset by large ultrasonic phase changes caused by the proximity of the heat source. This is another confirmation that the resolution of this system is limited by the phase noise caused by poor SNR on the periphery of the fan beam. The temperature rise near the central maxima in figure 10 is resolved to a few tenths of a millikelvin, comparable in magnitude to the noise in the raw (i.e. pre-averaged) waveforms obtained with the mono-channel, DPM system comprising the present instrument. Accordingly, incorporating similar signal averaging should improve the temperature resolution of the system.

The dynamic response of this system was assessed through another set of tests, designed to derive information about heat redistribution within the water tank as a function of time. As noted above, the system was limited to a minimum repetition period of 4 s, while spatial blurring of the temperature distributions due to heat conduction was not expected to exceed pixel dimensions of about 5 mm for times less than about 40 s. Thus, with the radiation beam directed along the vertical axis of the tank, we acquired a sequence of scans at 15 s intervals to see how well the results would conform to expectations based upon heat-transport theory.

The temperature distributions shown in figure 11(*a*), constructed similarly to those in figure 10, illustrate the accumulation of heat within the tank over a 90 s period of illumination. A plot of peak maxima as a function of time is shown in figure 11(*b*). The trend of the points in figure 11(*b*) with time indicates a rapid initial growth of temperature within the first 45 s followed by a period in which growth slows and reaches an apparent saturation condition by 90 s. According to the heat equation, such a levelling off of the

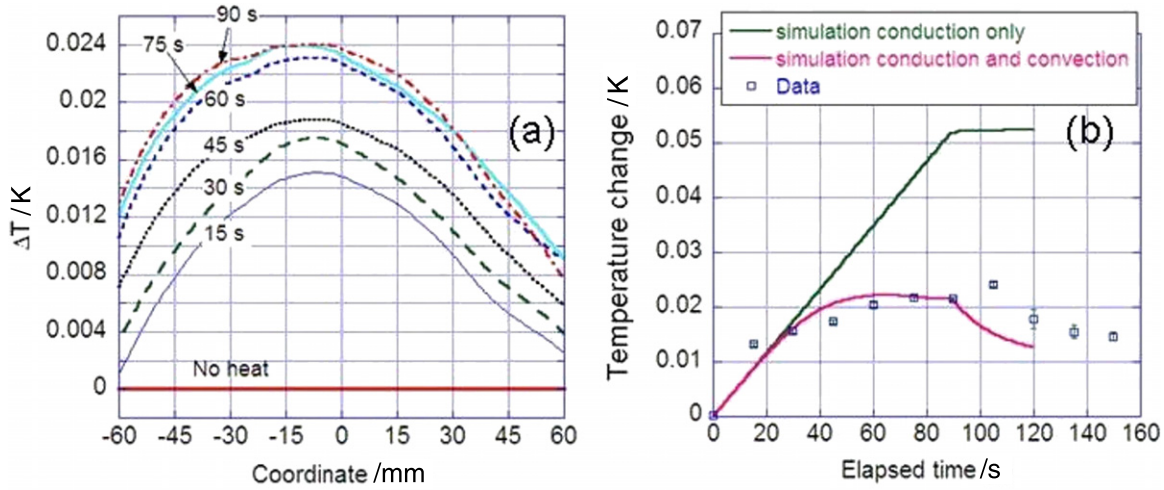

Figure 11. Time dependence of radiation-induced thermal distributions. (*a*) Successive temperature profiles (referenced to the no-heat profile) taken at approximately 15 s intervals while the beam is on; (*b*) time dependence of the temperature change of the central pixel.

temperature with time would occur if the second derivative of the temperature profile were to become sufficiently large, such that $\nabla^2 T \approx Q/k$, where k is the thermal conductivity of water ($0.6\,\mathrm{W\,m^{-1}\,K^{-1}}$) and Q is the heat power density ($1\,\mathrm{mW\,cm^{-3}}$ estimated for this experiment). The distributions in figure 11(*a*) suggest that $\nabla^2 T$ near each centroid is of order $1\,\mathrm{K\,m^{-2}}$, whereas Q/k in the detection volume during the experiment was nearly $1670\,\mathrm{K\,m^{-2}}$; thus, $\nabla^2 T \ll Q/k$, and heat conduction alone would not seem to be able to account for the levelling off shown in figure 11(*b*).

This conclusion is further supported by the output of a simple finite-element model of heat conduction in a cylindrical water tank. Using COMSOL Multiphysics software, we simulated the time evolution of temperature in a cylindrical body of water subjected to a heat source whose geometry and intensity resembled what was employed in the experiment: geometry of the source was made to be coaxial with the simulated tank, with a similar radius and a Lambert–Beer-like attenuation of intensity with depth that resulted in a $\sim 1\,\mathrm{mW\,cm^{-3}}$ average heating power at 10 cm depth. The output of this simulation, also plotted in figure 11(*b*), indicates a nearly linear increase in temperature with time, suggesting that conduction losses are negligible at such small illumination times.

Since earlier work with our mono-channel system in ionizing radiation with similar heating characteristics in a similar water tank had shown clear evidence of natural convection [5], we expected to see better agreement between simulation output and experimental data by including the incompressible Navier–Stokes equations in the model. The corresponding plot, shown in figure 11(*b*), exhibits the experimentally observed levelling off of temperature with time, although the simulation does not adequately characterize the rapid initial rise or the behaviour of the trend after the source is turned off. The semi-quantitative agreement with experiment obtained from this simple model nevertheless suggests that our prototype system is capable of real-time remote monitoring of radiation-induced temperature profiles in a water tank.

4. Conclusions

Experimental results obtained with the ultrasonic temperature profile visualization system demonstrate the feasibility of time-resolved measurements of sub-millikelvin temperature changes in water and, through tomographic reconstruction, the ability to create spatial/temporal maps of the evolving thermal profile in water subjected to an outside radiation heating event. Our instrument, based on a multiplexed 128-element circular ultrasonic array, obtains temperature maps from a cylindrical water tank with ~5 mm spatial resolution and sub-millikelvin sensitivity in pseudo-real-time (every 4 s). In the current implementation, the ultrasonic transducers are submerged in the water, but the array is wider than the diameter of the radiation beam and does not interfere with it. The system can monitor temporal evolution of spatial temperature distributions in water in a completely non-invasive way.

The spatial resolution can be improved by increasing the number of transducers in the array. Suggested improvements in the temperature and temporal resolutions are summarized below. All three resolutions are correlated to an extent; an improvement of one can come at the expense of the other.

The single-channel, DPM system [5] upon which the present system is based, has demonstrated a capability to resolve temperature changes of a few microkelvin using a special phase-detection algorithm followed by signal averaging. However, certain shortcomings of the present implementation prevented us from realizing its full potential. Part of the difference in performance may be attributable to the additional amplitude noise in the acquired waveforms, but much of it is likely due to the absence of signal averaging. The following areas of improvement are envisioned to achieve a temperature resolution of 10 μK or better: (1) the principal source of noise in the amplitude would seem to be switching noise (exhibited in figure 7(*a*)); however, because its frequency distribution lay mostly (if not entirely) outside the narrow bandwidth containing the signal of interest, we were able to eliminate much of that via digital filtering. Nevertheless,

since we cannot rule out the possibility that significant noise power resided within the signal bandwidth or that some (presumably small) phase distortion was introduced by the digital filter, eliminating the source of the switching noise would be desirable. (2) As noted, the remaining noise in the temperature waveforms was comparable in magnitude to that observed in the DPM raw waveforms prior to signal averaging, which was not implemented here because the present system could not handle the increased data throughput requirements. Considerable increases in throughput (two to three orders of magnitude) could be realized by parallelizing data acquisition from different array elements and incorporating dedicated processors for buffering and averaging data from the digitizer. (3) Subsequent increases in pulse repetition rate combined with higher-resolution ADCs and higher-precision clocks for triggering and synchronization are expected to enable us to approach if not exceed the resolution obtained with the DPM. (4) In addition, improvements to the spatial uniformity of fan beams generated by the transducers comprising the array would address the reduced signal-to-noise observed near the periphery of the beam that currently caused the reduction of the useful radius of the tomographic reconstruction window from 177.8 mm to less than 60 mm.

The temporal resolution, currently limited to one frame every 4 s, is adequate for slow variation of the temperature distributions due to heat exchange with the exterior environment as well as heat conduction and convection in the water due to radiation dose gradients. In the case of our single-channel thermometer, correcting for these effects is done by detrending the temperature history data or by using periodic heating and frequency-domain analysis. Adapting such techniques for the present instrument is expected to be straightforward and is planned for the next-generation prototype. For a faster changing dynamic environment, a solid-state switch with a higher switching speed can effectively decrease the image acquisition time to sub-seconds with the present array, making the system more directly applicable to the dynamic monitoring of radiation beam profiles and absolute absorbed dose measurements in water in some clinical conditions.

These results can be generalized to the mapping of temperature distributions in water as a result of any source of heating, presenting the potential for dosimetry standards in 3D for ionizing radiations including gamma photons and particle beams commonly used in radiation therapy and industrial applications. Unlike other dosimetry media (e.g. film or gel) in which radiation-induced changes are structural and permanent, the temperature change in water is transient and reversible. It is attractive to be able to obtain an instantaneous temperature map that refreshes in real time, and thereby able to directly realize the absorbed dose in water, without placing non-water materials in the beam (e.g. ion chambers or solid state detectors). In principle, a much further refined instrument based on these preliminary results can be developed into a 'universal standard dosimeter' for various radiation beams at temporal, spatial and thermal resolutions approaching 1 s, 1 mm and 1 μK, respectively.

Acknowledgments

The authors would like to express their sincere gratitude to Bryan Hefner for electronics design and fabrication; to Dr Mark McKenna for acoustic lens suggestion; to David Coombs, Albert Sanford and Anjani Achanta for ultrasonic array fabrication.

This research has been supported by NIST contracts SB1341-04-W-1127 and SB1341-05-C-0025.

Disclaimer

Identification of certain commercial equipment, instruments or materials in this document does not imply recommendation or endorsement by the NIST, nor does it imply that the products identified are necessarily the best available for the purpose.

References

[1] Webb S 2003 The physical basis of IMRT and inverse planning *Br. J. Radiol.* **76** 678–89
[2] Domen S R 1994 A sealed water calorimeter for measuring absorbed dose *J. Res. Natl Inst. Stand. Technol.* **99** 121–41
[3] Malyarenko E, Heyman J, Guy S, Chen-Mayer H and Tosh R 2006 Absorbed radiation dose measurement with a μK-resolution ultrasonic thermometer *Med. Phys.* **33** 2292
[4] Malyarenko E, Heyman J, Guy S, Tosh R and Chen-Mayer H 2005 An ultrasonic high-resolution thermometer for radiation dosimetry *Biomedical Imaging Research Opportunities Workshop 3 (Bethesda, MD, 11–12 March 2005)*
[5] Malyarenko E, Heyman J, Chen-Mayer H and Tosh R 2008 High-resolution ultrasonic thermometer for radiation dosimetry *J. Acoust. Soc. Am.* **124** 3481–90
[6] Heyman J S and Malyarenko E V 2008 Dynamic acoustic thermometer *US Patent* 7404671, 07/29/2008
[7] Papadakis E P (ed) 2000 *Ultrasonic Instruments and Devices* (New York: Academic)
[8] Green S F 1985 An Acoustic technique for rapid temperature distribution measurement *J. Acoust. Soc. Am.* **77** 759–63
[9] Athanassoulis G A and Skarsoulis E K 1995 Arrival-time perturbations of broadband tomographic signals due to sound-speed disturbances. A wave-theoretic approach *J. Acoust. Soc. Am.* **97** 3575–88
[10] Skarsoulis E K, Send U, Piperakis G and Testor P 2004 Acoustic thermometry of the western Mediterranean basin *J. Acoust. Soc. Am.* **116** 790–8
[11] Fife S, Andereck C D and Rahal S 2003 Ultrasound thermometry in transparent and opaque fluids *Exp. Fluids* **35** 152–8
[12] Mather M, Whittaker A and Baldock C 2002 Ultrasound evaluation of polymer gel dosimeters *Phys. Med. Biol.* **47** 1449–58
[13] Mather M, Charles P and Baldock C 2003 Measurement of ultrasonic attenuation coefficient in polymer gel dosimeters *Phys. Med. Biol.* **48** N269–75
[14] Mather M and Baldock C 2003 Ultrasound tomography imaging of radiation dose distributions in polymer gel dosimeters *Med. Phys.* **30** 2140–8
[15] Palanichamya P and Radhab E 2008 Radiation dose measurements in irradiated PMMA using ultrasonic technique *Radiat. Meas.* **43** 1319–23
[16] Li C, Duric N and Huang L 2008 Breast imaging using transmission ultrasound: reconstructing tissue parameters of sound speed and attenuation *Int. Conf. on BioMedical Engineering and Informatics BMEI (Sanya, Hainan, China)* pp 708–12

[17] Kak A S and Slaney M 1988 *Principles of Computerized Tomographic Imaging* (New York: IEEE)
[18] Lubbers J and Graaff R 1998 A simple and accurate formula for the sound velocity in water *Ultrasound Med. Biol.* **24** 1065–8
[19] Carslaw H S and Jaeger J C 1986 *Conduction of Heat in Solids* 2nd edn (Oxford: Clarendon)
[20] Hale G M and Querry M R 1973 Optical constants of water in the 200-nm to 200-micrometer wavelength region *Appl. Opt.* **12** 555